3D-printing for the precision assessment of a new medical device

Francesca COSMI[1], Alberto DAL MASO[1] and Giorgio ZATTA[2]

Abstract

Additive manufacturing played a keyrole in investigating the precision of a recently-developed device that measures the elastic characteristics of the trabecular bone by simulating the application of loads on a virtual biopsy obtained from radiographic images of the proximal epiphyses in the patient's hand fingers. The simulation results are combined in a Bone Structure Index (BSI), which has shown to be able to detect trabecular bone alterations due to osteoporosis or other pathological situations. In order to obtain a large number of measurements without having voluntary patients undergo unnecessary radiations, the precision assessment tests were carried out on a 3D-printed phantom hand, in which different mimicked trabecular structures *(chips*) were inserted. Each mimicked bone had a unique internal structure and density and was 3D-printed using radiopaque composite materials. Fifteen different chips were additively manufactured; 20 measurements were performed on each chip. BSI and BSI_T-score precision values were computed according to ISO 5725 and ISCD standards. For all the chips, no relationship was found between the mean m_j and standard deviation s_j of the measurements in each chip. The range of the 95% confidence interval (*CI*) was computed assuming the repeatability standard deviation s_r as the known standard deviation of the measurement method (average of s_j values): $CI_{BSI} = \pm 8.14$, corresponding to $CI_{Tscore} = \pm 0.36$. Least Significant Change was evaluated as well: $LSC_{BSI} = 13.1$, corresponding to $LSC_{Tscore} = 0.58$. The 95% confidence intervals are small when compared to the commonly-accepted diagnostic values, where a patient is classified as osteoporotic if T-score < -2.5, non-osteoporotic if T-score $>$ -1 and osteopoenic if -2.5 $<$ T-score $<$ -1. The LSC results are in line with the requirements for the gold-standard osteoporosis diagnostic systems. Additive manufacturing made it possible to avoid irradiation of humans in this precision assessment.

Keywords

3D printing, BEStest, bone, measurement, reliability analysis, phantom study

Accepted: 27 February 2021

Introduction

Diagnosis of fragility fracture risk is usually based on Bone Mineral Density (BMD). The gold standard for BMD measurements is Dual Energy X-ray Absorptiometry (DEXA). However, it has been widely reported that BMD is not always sufficient as a single diagnostic method for fracture risk assessment, as it does not take into account the architectural elasticity (or quality) of the trabecular arrangement, which explains up to 40% of the bone's overall load-bearing capability.[1–4] In fact, studies have shown a significant overlap in BMD between fractured and healthy subjects.[5–9] Moreover, there are several cases in which an increase in fracture risk can be observed despite an increase in BMD, for example in individuals with type 2 diabetes, rheumatoid arthritis or lumbar disk degeneration.[10–12]

Algorithms such as FRAX™, DeFRA™ and QFracture™ have been developed to recognize individual fracture risk based on risk factors such as age, gender, prior fractures, family history, lifestyle, as well as BMD T-score when available.[13–17] These algorithms have been adopted as prescribability criteria for medical treatment, but they are not diagnosis or monitoring tools.[18] Alternative quantitative imaging methods include trabecular bone score (TBS),

[1]Department of Engineering and Architecture, University of Trieste, Trieste, Italy
[2]Centro radiologico Giuliano, Trieste, Italy

quantitative ultrasound (QUS), computed tomography (CT), high-resolution (HR) MRI, positron emission tomography (PET): their employment in supporting clinical decisions is currently field of research.[19–24]

The Bone Elastic Structure Test (BES TEST™) is a recently-developed technique for the evaluation of the elastic characteristics of trabecular bone through numerical simulations consisting in the application of loads on a virtual biopsy of the patient, obtained from radiographic images of the proximal epiphyses in the patient's hand fingers. These radiograms are obtained by means of a handheld portable X-ray system coupled with a digital sensor: this procedure is simple and the amount of ionizing radiations both to the patient and to the operator is exceptionally low. The BES TEST™ results in an index, the *Bone Structure Index* (BSI), that summarizes the elastic behavior and, therefore, the load-bearing capability of the trabecular part of the bone. A thorough description of this method is beyond the scope of this paper; details can be found in literature.[25–35]

By directly evaluating the bone's response to loads, BES TEST™ has shown the potential for representing an effective exam for the early diagnosis of pathological alterations of the bone microarchitecture.[28,30,31] BES TEST™ monitors exclusively the trabecular bone, which changes much more rapidly than cortical bone and than BMD in response to physio-pathological alterations. Moreover, BES TEST™ is fast, easy to perform, cost-effective and does not require the patient to undergo any specific preparation. For these reasons, BES TEST™ can be repeated regularly and at short time intervals to closely monitor the patient's condition over time. Pilot studies have shown that the integration of BMD and BES TEST™ can represent an effective solution for the assessment of the overall bone fracture risk and patient follow-up.

This work aims at quantifying the precision of BES TEST™ under *repeatability conditions* (described in the following section), to evaluate the consistency of this measuring method and its internal variability. The ISO 5725 norm was followed[36–38] and the range of the 95% Confidence Interval (*CI*) was calculated.[39] The Least Significant Change (LSC) between two successive measurements was also evaluated, following the guidelines recommended by the International Society for Clinical Densitometry (ISCD), which can be applied to any sort of measurement.[40–42]

In order to collect a large amount of data without having patients undergo unnecessary radiation, the tests for this study were performed on a 3D-printed phantom hand, inside which various radiopaque *chips* were inserted. Different combinations of Fused Deposition Modelling (FDM) and Stereolitography (SLA) technologies were used in this applicatiom to mimic different trabecular bone structures, as detailed in the following section for each *chip* type. The great popularity of FDM is mostly due to its low cost, which compensates for its dimensional inaccuracies, mainly caused by heat warping and incomplete adhesion of the filament layers. Fused Deposition Modeling by a Builder Premium Medium™ 3D printer was used in the A and D type *chips*.[43–45] Stereolithography is becoming a very interesting alternative to FDM as it produces parts with a greater overall dimensional accuracy and a better surface finish, albeit at a somehow higher cost; a Formlabs™ Form 2™ SLA printer was used for the production of both the phantom hand and type A, B, C and D *chips*.[46–48]

Methods

Phantom hand and chip design

An open right-hand 3D model meeting the characteristics of the average BES TEST™ patient was obtained from an oline CAD sharing platform[49] and was further edited on Blender™ 3D graphic software. A slot was carved in the proximal phalanges of the index finger, where different mimicked bone structures (chips) were inserted. The phantom hand was then 3D printed in a Formlabs™ SLA 3D printer using Clear V4™ transparent resin; this material has a radiopacity similar to that of human soft tissue, making it particularly suitable for this application. Due to material cost and availability, only the actually radiographed volume was printed: from the knuckle to the middle interphalangeal crease of the index finger (Figure 1).

In a preliminary phase, aimed at finding the best manufacturing methods and parameters for the mimicked chips, 48 chips were additively manufactured, and 1080 acquisitions were performed. Finally, 15 chips were 3D printed for the repeatability assessment. All chips are 32×29 mm (length $\times$ width), while their height differs from type to type. The chips can be classified as belonging to one of four types, Table 1.

Type-A chips. A rectangular 2-mm-thick structure was SLA 3D-printed using Clear V4™ resin and a 0.3-mm-deep bone-shaped engraving was carved on one face. The mimicked bones were 3D-printed using FMD technology with ColorFabb™ BronzeFill™: a composite material made of bronze particles (35% v/v) in a Poly-Lactic Acid (PLA) matrix. BronzeFill™ is highly radiopaque, therefore 0.2 mm of thickness produced an image with similar chromatic contrast to a standard 15-mm-thick bone. The FDM layer height was fixed to 0.1 mm, while infill density and pattern were adjusted to obtain different internal structures, and therefore different BSI values. The main drawback of this technique was the limited geometrical complexity achievable by the FDM 3D printer on such small parts. Since the

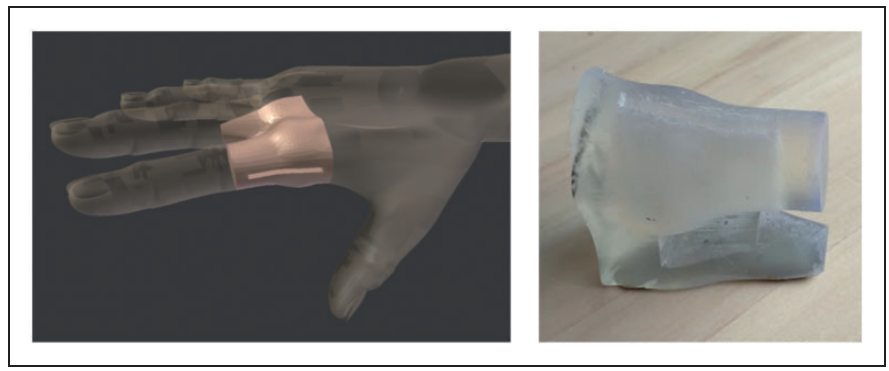

Figure 1. Phantom hand design. Left: CAD drawing, 3D-printed portion highlighted. Right: 3D-printed phantom.

Table 1. Number of 3D printed chips in each category.

	Type A	Type B	Type C	Type D	Total (q)
Number of chips	5	4	2	4	15
3D printing technology	FDM+SLA	SLA	SLA	LA	

height-to-width ratio is very small, type-A chips are essentially 2-dimensional (Figure 2).

Type-B chips. These chips were made entirely by SLA with a layer height of 25 μm, making the most out of the extremely high geometrical resolution of this 3D-printing technology. The starting point was a greytone image of a bone, be it a radiograph on a real patient or any similar artificial image. This was interpreted as a linear height field using a 3D graphic software and subtracted to the plain 2-mm-thick rectangular chip, so that brighter portions resulted in deeper engravings and viceversa. Once 3D-printed, this chip type acts as a mould for a radiopaque filling: the BronzeFill™ raw material was chosen for this purpose. The bronze particle size is sufficiently small (10-30 μm) when compared to the printing resolution (50-100 μm) to guarantee an adequate image detail. When a type-B chip is radiographed, areas with a deeper engraving (i.e. thicker radiopaque infill) result in brighter areas on the image, and viceversa. With this method, any greytone or b/w bone image can be reproduced, as well as any shape, be it geometrical or organic. The main limitation of this procedure is again the printing resolution: this becomes an issue particularly when working with shades of gray, while for black-or-white images it proves more detailed and reproducible than type-A (Figure 3).

Type-C chips. Three type-B chips were piled up to form a type-C chip (Figure 4). These have an overall thickness of 6 mm (3×2 mm) and a more complex structure that can be fully considered 3-dimensional. In this case, the infill geometry was chosen among the simplified trabecular models used for the method validation in Cosmi.[32]

Type-D chips. These fully 3D chips were created using both FDM and SLA. The base was a 6-mm-thick resin chip with a bone-shaped slot. A BronzeFill™ bone contour was FDM 3D-printed and then inserted in the resin. The free central volume was filled with copper wire (0.25 mm diameter), which was randomly laid out in all three directions of space. The result mimics the organic 3D structure of trabecular bone (Figure 5). Different densities and layouts of the copper wires lead to different BSI values.

BES TEST™ technique

One full BES TEST™ analysis consists of three *acquisitions* of radiographic images (AP projection) of the proximal epiphysis in the index, middle and ring finger of the non-dominant hand. These images are obtained with a handheld portable X-ray system coupled with a digital sensor (acquisition parameters: KVP 60, exposure 0.17 s).[50] While the trained operator acquires the images on the patient's open hand, the patient is reasonably still. The radiation source is positioned on the back of the hand, while the sensor is held on the palm and aligned with the radiation beam (Figure 6).

The radiographic images are then uploaded to the BES TEST™ website, where they are processed and analysed on the cloud. The analysis of each image can be divided into two main steps.

- Definition of the *Region Of Interest* (ROI): a dedicated algorithm identifies the portion of the image that will be analysed.
- Mechanical simulation: using a Cell Method numerical model of the ROI, the apparent elastic moduli along different directions are calculated. These results are then summarized in an adimensional index – the *Bone Structure Index* (BSI) – which represents the load-bearing capability of

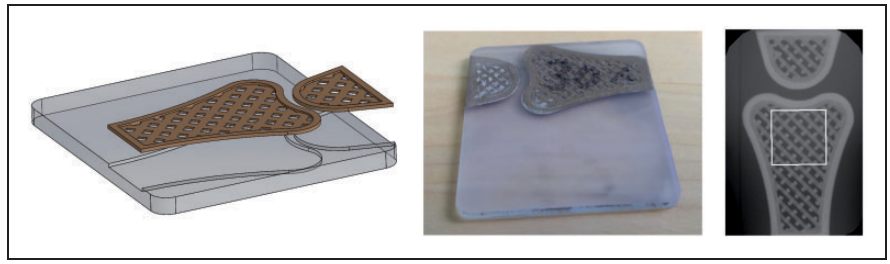

Figure 2. Type-A chips. Left: CAD drawing. Center: 3D printed chip. Right: radiogram.

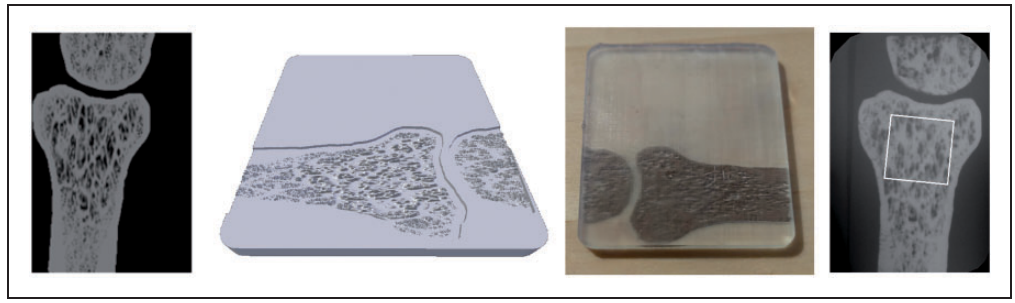

Figure 3. Type-B chips. (a) Starting image; (b) CAD drawing; (c) 3D printed chip; (d) radiogram.

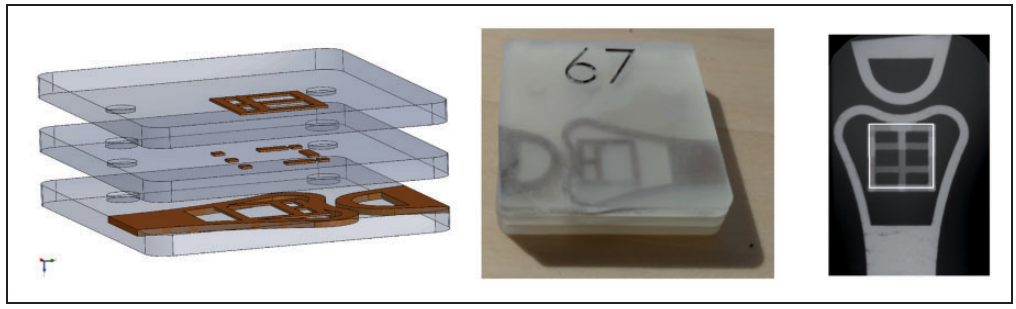

Figure 4. Type-C chips. Left: CAD drawing. Center: 3D printed chip. Right: radiogram.

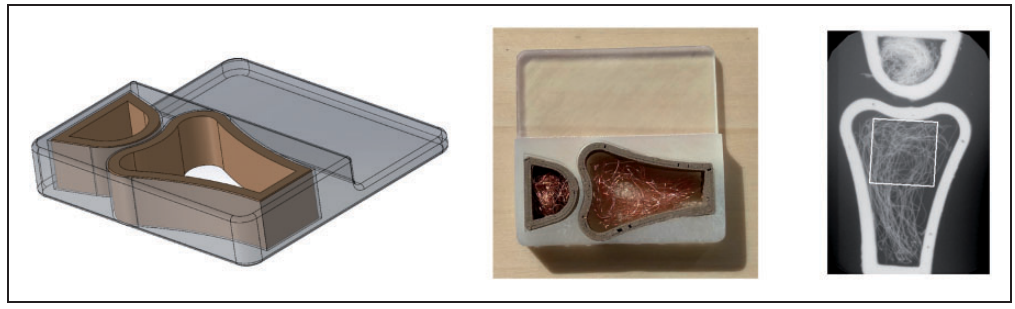

Figure 5. Type-D chips. Left: CAD drawing. Center: 3D printed chip and copper wiring. Right: radiogram.

the structure reconstructed from the analysed trabecular region. Details can be found in literature.[26,27,51,52]

The BSI values can be then converted into a T-score, commonly adopted also for BMD measurements

$$Tscore = \frac{BSI - \mu}{\sigma} \quad (1)$$

Where μ and σ are – respectively – the mean and standard deviation BSI of the young population. These values have been obtained in a previous study.[39] By definition, T-score is an adimensional quantity. In analogy with the common practice in BMD measurements, diagnosis is based on T-score values. The adopted thresholds are the same used for BMD: a T-score >-1 indicates no risk of bone disease, a T-score <-2.5 suggests full-blown

Figure 6. BES TEST™ procedure on a real patient. Left: radiographic acquisition. Right: acquired radiographic image to be analysed.

pathological conditions, while if $-2.5 < \text{T-score} < -1$ the patient is considered worth of monitoring for further assessment.

Design of experiments

All replicate measurements were performed under *repeatability conditions*, as defined by the International Vocabulary of Metrology, that is: *replicate measurements on the same or similar objects over a short period of time, using the same measurement procedure, the same operator, the same measuring system, the same operating conditions and the same location*.[53] Therefore, as explicitly recommended by the norm, there was no repositioning between successive acquisitions on the same chip. All tests were performed at a private radiological centre, by a single specifically-trained operator.

The 3D-printed hand was placed on a support, in the approximate position of the patient's hand during a BES TEST™ acquisition. The RX source was held in contact with the table for greater stability; the operator was standing.

On each chip, 20 acquisitions were performed, for a total of 300 radiographs. The BSI value was recorded for each acquisition and the method's overall repeatability standard deviation s_r was calculated following ISO 5725 – *Accuracy (trueness and precision) of measurement methods and results*.[36] Once verified that the results for each chip follow a normal distribution, the 95% confidence interval was calculated.

Precision assessment: Results and discussion

95% confidence interval

BSI values for each acquisition are reported in Figure 7. Mean and standard deviation were calculated for each of the $q = 15$ chips (or *levels*). There appears to be no evident relationship between the mean and the variance throughout the levels, therefore the repeatability standard deviation s_r is given by the mean of the standard deviations for each level

$$s_r = \frac{\sum_{j=1}^{q} s_j}{q} \tag{2}$$

Table 2 shows the mean and mean standard deviation for each chip type, as well as the overall mean and s_r throughout all 15 levels.

Ten different normality tests were performed for each level, including Kolmogorov-Smirnov (KS) test and its modifications, Shapiro-Wilk, Cramer-Von Mises, Shapiro-Francia and other less popular ones.[54] Results of the tests per chip are reported in Table 3 and confirm the normality assumption. The following formula can be applied to calculate the 95% confidence interval for each chip, remembering that each BES TEST™ analysis is made of three averaged acquisitions and that

$$CI_{BSI} = 2 \times 1.96 \frac{s_r}{\sqrt{n}} \tag{3}$$

where CI_{BSI} is the range of the 95% confidence interval computed from BSI values and $n = 3$ is the number of repeated measurements.

Least significant change

The Least Significant Change (LSC) is often considered when repeated measurements are performed on the same person at (relatively) large time intervals, with the intent to monitor the evolution of a certain disease and its response to therapy. This concept is widely used in BMD measurements and can be applied also to BSI. The LSC is defined as the least amount of change between two measurements over time that must be exceeded before a change can be considered true (with 95% confidence). If the absolute difference is less than the LSC, this is most likely due to the internal variability of the measuring method and is not an index of real biological change.

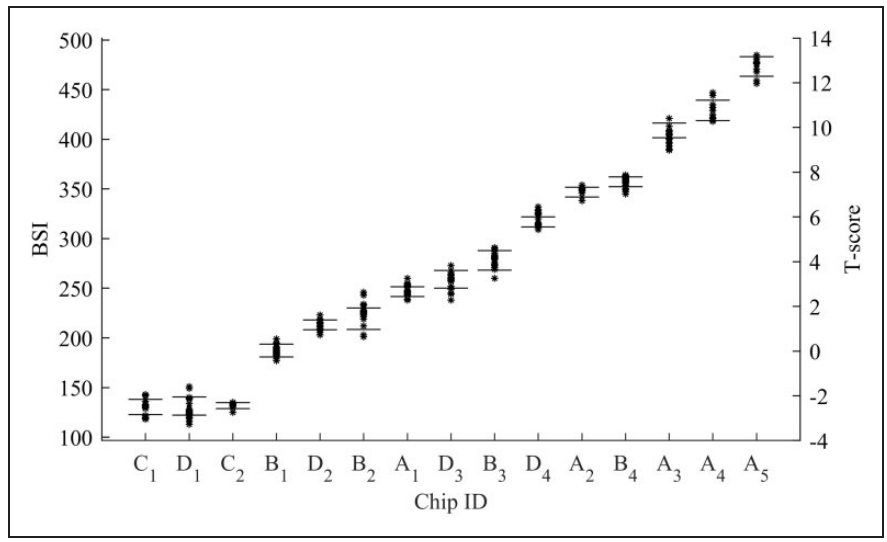

Figure 7. Test results for each chip. Error bars: mean ± std. dev. Right y-axis: BSI results converted to T-score.

Table 2. Mean BSI and mean standard deviation for each chip type.

	Type A	Type B	Type C	Type D	Overall
Mean	381	261	131	230	275
Mean variance	7.47	7.37	5.33	7.75	7.19

Table 3. Results for the normality tests on each chip. 1 = passed; 0 = not passed (p = 0.05).

	A_1	A_2	A_3	A_4	A_5	B_1	B_2	B_3	B_4	C_1	C_2	D_1	D_2	D_4	D_5
KS Limiting Form	1	1	1	1	1	1	1	1	1	1	1	1	1	1	1
KS Stephens Mod.	0	1	1	1	1	1	1	1	1	1	1	1	1	0	1
KS Marsiglia	1	1	1	1	1	1	1	1	1	1	1	1	1	1	1
KS Lilliefors Mod.	0	1	1	1	1	1	1	1	1	1	1	1	1	0	1
Anderson–Darling	1	1	1	1	1	1	1	1	1	1	1	1	1	1	1
Cramer–Von Mises	1	1	1	1	1	1	1	1	1	1	1	1	1	1	1
Shapiro–Wilk	1	1	1	1	1	1	1	1	1	1	1	1	1	1	1
Shapiro–Francia	1	1	1	1	1	1	1	1	1	1	0	1	1	1	1
Jarque–Bera	1	1	1	1	1	1	1	1	1	1	1	1	1	1	1
D'Agostino–Pearson	1	1	1	1	1	1	1	1	1	1	0	1	1	1	1
Total (/10)	8	10	10	10	10	10	10	10	10	10	8	10	10	8	10

The LSC for the BES TEST™ procedure was evaluated following the ISCD guidelines applied to the phantom patients. The ISCD recommends calculating the LSC with triplicate measurements on at least 15 patients. Thanks to the large number of available measurements in this study, the LSC was evaluated using all the 20 repeated measurements for each chip: this sample is larger than required, thus has an even greater statistical reliability. Since a complete BES TEST™ analysis consists of $n = 3$ averaged acquisitions, the calculated LSC is divided by $\sqrt{n} = \sqrt{3}$. This is equivalent to grouping the acquisitions in triplets and performing the LSC calculations on their average.

The Root Mean Squared Standard Deviation ($RMS\ SD$) among the $q = 15$ chips is calculated as

$$RMS\ SD = \sqrt{\frac{\sum_{j=1}^{q} (SD_j)^2}{q}} \tag{4}$$

where SD is the standard deviation of the 20 repeated measurements for each chip. The LSC is obtained as

$$LSC_{BSI} = \frac{1.96 \times \sqrt{2} \times RMS\ SD}{\sqrt{n}} \tag{5}$$

Where again $n = 3$ is the number of repeated measurements of a complete BES TEST™ exam.

Both the CI and the LSC were calculated in BSI units and converted to T-score units; Table 4 summarizes the results.

Discussion

Although BES TEST™ and DEXA do not measure the same quantity, in order to interpret the obtained results and to understand the order of magnitude of the calculated variability, it may be useful to compare the standard precision of common state-of-the-art DEXA setups with that of the recently-developed BES TEST™. The LSC will be used as reference, but it must be converted to adimensional T-score units in order to perform this comparison.

BMD readings on a patient can vary quite considerably depending on the scanned area (lumbar spine, total hip, femoral neck), on the machine model used and the radio-technologist's skill; DEXA systems are required to guarantee an overall relative precision error ($PE_{BMD,rel}$) on repeated measurements of 1.9∼2.5% depending on the scanned area.[55] To convert this to T-score, let us consider the average population BMD for Caucasian women, age <35 years, as reported in the NHANES database.[54,56–58]

$$\mu_{BMD} = 0.94\,\mathrm{g/cm^3} \tag{6}$$

The required precision error (PE) can be expressed in absolute terms by multiplying the relative precision error ($PE_{BMD,rel}$) by the average BMD

$$PE_{BMD} = PE_{BMD,rel} \times \mu_{BMD} \approx 0.017 \sim 0.023\,\mathrm{g/cm^3} \tag{7}$$

This corresponds to a maximum acceptable LSC of

$$\mathrm{LSC}_{BMD} = PE_{BMD} \times 2.77 \approx 0.050 \sim 0.065\,\mathrm{g/cm^3} \tag{8}$$

Assuming a typical population variance $\sigma_{\mathrm{BMD}} \approx 0.12\ \mathrm{g/cm^3}$, again as reported in the NHANES database, the LSC can be expressed in terms of T-score

$$LSC_{BMD,\ Tscore} = \frac{LSC_{BMD}}{\sigma_{BMD}} \approx 0.4 \sim 0.6 \tag{9}$$

This value can be compared to the LSC for BES TEST™, which was evaluated at 0.58 T-score: therefore, in the same range as that of a gold-standard test for the diagnosis of bone diseases. This is an excellent result considering the low cost and low radiation dose associated with BES TEST™ technology.

Finally, Figure 8 shows the results of the BES TEST™ analyses on six patients who for various reasons had the BES TEST™ performed twice. The error bars indicate the previously calculated confidence intervals. Different colors represent different areas of risk in relation to the accepted threshold values. All duplicate results lie within the expected confidence interval, thus confirming the validity of the results obtained on the 3D-printed chips.

Table 4. CI and LSC obtained from the BES TEST™ measurements on the chips.

CI_{BSI}	CI_{Tscore}	LSC_{BSI}	LSC_{Tscore}
16.3	0.73	13.1	0.58

Conclusions

The precision assessment carried out in this work was performed on a 3D-printed phantom hand, in which different 3D printed mimicked trabecular structures

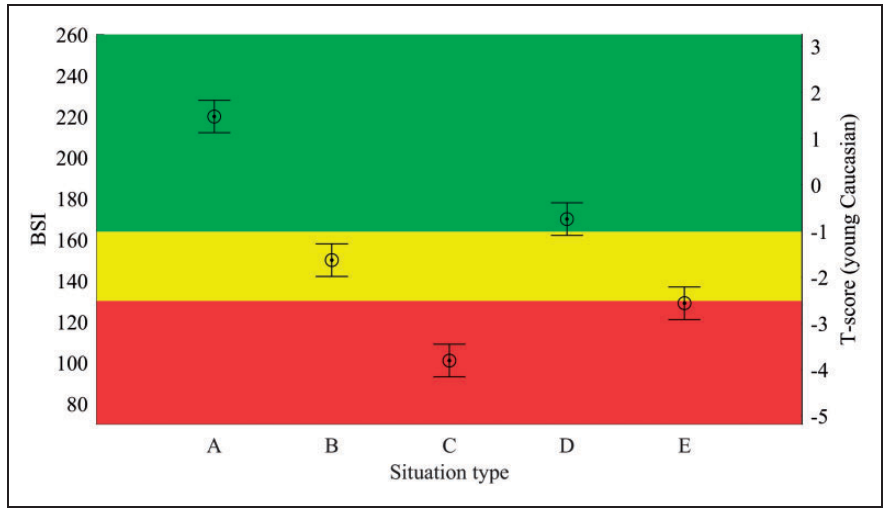

Figure 8. Duplicate BES TEST™ measurements on six real patients. Error bars: expected CI.

(*chips*) were inserted. Each mimicked bone had a unique internal structure and density and was 3D-printed using radiopaque composite materials. This allowed to perform a large number of repeated acquisitions without exposing patients to extra doses of ionizing radiation, thus gaining a solid understanding of the consistency of repeated BSI measures without an increased radiation risk.

Although the internal structure of the mimicked bones has the same radiographic characteristics of that of bone tissue, the correspondence of these results with those of similar tests performed on real patients is yet to be investigated. The next step will be to evaluate the variability under *reproducibility conditions*, i.e. same measurand, same methodology, but different operator and location.

Acknowledgments

The authors thank the six patients whose BES TEST™ results are shown in Figure 8.

Declaration of Conflicting Interests

The author(s) declared no potential conflicts of interest with respect to the research, authorship, and/or publication of this article.

Funding

The author(s) received no financial support for the research, authorship, and/or publication of this article.

ORCID iD

Francesca COSMI https://orcid.org/0000-0002-0191-2664

References

1. Kleerekoper M, Villanueva A, Stanciu J, et al. The role of three dimensional trabecular microstructure in the pathogenesis of vertebral compression fractures. *Calcif Tissue Int* 1985; 37: 594–S597.
2. Barou O, Valentin D, Vico L, et al. High-resolution three-dimensional microcomputed tomography detects bone loss and changes in trabecular architecture early: comparison with DEXA and bone histomorphometry in a rat model of diuse osteoporosis. *Invest Radiol* 2002; 37: 40–46.
3. Ruppel M, Miller L, and Burr D. The effect of the microscopic and nanoscale structure on bone fragility. *Osteoporos Int* 2008; 19: 1251–1265.
4. Small RE. Uses and limitations of bone mineral density measurements in the management of osteoporosis. *Medscape Gen Med* 2005; 7.
5. Friedman A. Important determinants of bone strength: beyond bone mineral density. *J Clin Rheumatol* 2006; 12: 70–77.
6. Bogado CBq. *Postmenopausal osteoporosis: hormones & other therapies*. Boca Raton, FL: CRC Press, 2016, pp. 97–101.
7. Wainwright S, Phipps K and Stone J. A large proportion of fractures in postmenopausal women occur with baseline bone mineral density t-score -2.5. *J Bone Miner Res* 2001; 16: S155.
8. Schuit S, van der Klift M, Weel A, et al. Fracture incidence and association with bone mineral density in elderly men and women: the Rotterdam Study. *Bone* 2004; 34: 195–202.
9. Kanis JA, McCloskey EV, Johansson H, et al. Development and use of FRAX® in osteoporosis. *Osteoporos Int* 2010; 21: 407–413.
10. Ma L, Oei L, Jiang L, et al. Association between bone mineral density and type 2 diabetes mellitus: a meta-analysis of observational studies. *Eur J Epidemiol* 2012; 27: 319–332.
11. Oei L, Rivadeneira F, Zillikens M, et al. Diabetes, diabetic complications, and fracture risk. *Curr Osteoporos Rep* 2015; 13: 106–115.
12. Castaño-Betancourt M, Oei L, Rivadeneira F, et al. Association of lumbar disc degeneration with osteoporotic fractures; the Rotterdam study and Meta-analysis from systematic review. *Bone* 2013; 57: 284–289.
13. Oka R, Ohira M, Suzuki S, et al. Fracture risk assessment tool (FRAX) and for the diagnosis of osteoporosis in Japanese Middle-aged and elderly women: Chiba bone survey. *Endocr J* 2018; 65: 193–202.
14. Dawson-Hughes B, Tosteson ANA, Melton LJ, et al. Implications of absolute fracture risk assessment for osteoporosis practice guidelines in the USA. *Osteoporos Int* 2008; 19: 449–458.
15. Browner WS. Predicting fracture risk: tougher than it looks. *IBMS BoneKEy* 2007; 4: 226–230.
16. Kanis JA, Oden A, Johnell O, et al. The use of clinical risk factors enhances the performance of BMD in the prediction of hip and osteoporotic fractures in men and women. *Osteoporos Int* 2007; 18: 1033–1046.
17. Rossini M, Adami S, Bertoldo F, et al. Guidelines for the diagnosis, prevention and management of osteoporosis. *Reumatismo* 2016; 68: 1–42.
18. N. O. G. Group. Clinical guideline for the prevention and treatment of osteoporosis, www.sheffield.ac.uk/NOGG/NOGG%20Guideline%202017.pdf (2018. accessed 21 October 2019).
19. Komar C, Ahmed M, Chen A, et al. Advancing methods of assessing bone quality to expand screening for osteoporosis. *J Am Osteopath Assoc* 2019; 119: 147–154.
20. Ayubcha C, Raynor W and Alavi WT. A evolving role of NaF-PET in the diagnosis and treatment of osteoporosis. *J Nucl Med* 2017; 58: 1007.
21. Oei L, Koromani F, Rivadeneira F, et al. Quantitative imaging methods in osteoporosis. *Quant Imaging Med Surg* 2016; 6: 680–698.
22. Silva B, Leslie W, Resch H, et al. Trabecular bone score: a noninvasive analytical method based upon the DXA image. *J Bone Miner Res* 2014; 29: 518–530.
23. Moayyeri A, Hsu Y, Karasik D, et al. Genetic determinants of heel bone properties: genome-wide association Meta-analysis and replication in the GEFOS/GENOMOS consortium. *Hum Mol Genet* 2014; 23: 3054–3068.
24. Di Paola M, Gatti D, Viapiana O, et al. Radiofrequency echographic multispectrometry compared with dual X-ray absorptiometry for osteoporosis diagnosis on lumbar spine and femoral neck. *Osteoporos Int* 2019; 30: 391–402.

25. Cosmi F, et al. The bone structure index: a study on bone quality. In: *Fourth international conference on mechanics of biomaterials & tissues*, Waikoloa Beach Marriott Resort, Hawaii, USA, 2015.
26. Cosmi F. Numerical solution of plane elasticity problems with the cell method. *Comput Model Eng Sci* 2001; 2: 365–372.
27. Cosmi F and Dreossi D. Numerical and experimental structural analysis of trabecular architectures. *Meccanica* 2007; 42: 85–93.
28. Cosmi F and Dreossi D. The application of the cell method in a clinical assessment of bone fracture risk. *Acta Bioeng Biomech* 2007; 9: 35–39.
29. Cosmi F. Morphology-based prediction of elastic properties of trabecular bone samples. *Acta Bioeng Biomech* 2009; 1: 3–9.
30. Cosmi F, et al. *A structural method for the clinical evaluation of fracture risk in osteoporosis*. In: Fourth International Conference on Mechanics of Biomaterials & Tissues, Waikoloa Beach Marriott Resort, Hawaii, USA, 2011.
31. Cosmi F and Mazzoleni G. Evaluation of the structural quality of bone in a case of progressive osteoporosis complicating a complex regional pain syndrome (CRPS) of the upper limb. *J Mech Behav Biomed Mater* 2014; 29: 517–528.
32. Cosmi F. Numerical evaluation of trabecular bone alterations: a cell method application. *Mol Cell Biol* 2015; 12: 87–105.
33. Cosmi F, Nicolosi A and Zatta G. Osteoporosis risk factors and bone microstructure evaluation: a population breakdown. *Mater Today: Proc* 2018; 5: 26772–26777.
34. Cosmi F and Nicolosi A. The bone structure index and the requirements for its evaluation with a hand-held x-ray imaging system. *Materials Today: Proceedingsb* 2018; 5: 26667–26672.
35. Saviola G, Sacco S and Saibene L, A-A. L. Bestest analysis in patients with normal or osteopoenic dexa. A case-control study. *Minerva Medica* 2019; 10: 597–599.
36. Accuracy (trueness and precision) of measurement methods and results. *ISO* 2004; 5725
37. JCGM, Evaluation of measurement data – Guide to the expression of uncertainty in measurement, 2008.
38. ISO/IEC 170252005. General requirements for the competence of testing and calibration laboratories.
39. Beretta S. *Affidabilità delle costruzioni meccaniche*. Milano: Springer Italia, 2009. pp. 31–36.
40. Shepherd JA and Lu Y. A generalized least significant change for individuals measured on different DXA systems. *J Clin Densitom* 2007; 10: 249–258.
41. Kawalilak C, Johnston J, Olszynski W, et al. Least significant changes and monitoring time intervals for high-resolution pQCT-derived bone outcomes in postmenopausal women. *J Musculosk Neuron Interact* 2015; 15: 190–196.
42. ISCD Precision Assessment, www.iscd.org/resources/calculators/precision-calculator/faq/ (accessed 15 October 2019).
43. Redwood B, Scöffer F and Garret B. *The 3D printing handbook*. Amsterdam: 3D Hubs B.V., 2018. pp. 53–72.
44. Cosmi F and Dal Maso A. Validation of an in-house-designed tensile testing machine for the mechanical characterization of 3D-printed specimens. *Proc IMechE, Part C: J Mechanical Engineering Science* 2019.
45. Dal Maso A and Cosmi F. Mechanical characterization of 3D-printed objects. *Mater Today: Proc* 2018; 5: 26739–26746.
46. Schmidleithner C and Kalaskar DM. Stereolithography in 3D printing. *IntechOpen* 2018, pp. 3–22.
47. Cosmi F and Dal MA. A mechanical characterization of SLA 3D-printed specimens for low budget applications. *Mater Today: Proc* 2020; 32: 194–201.
48. Saini JS, Dowling L, Kennedy J, et al. Investigations of the mechanical properties on different print orientations in SLA 3D printed resin. *Proc IMechE, Part C: J Mechanical Engineering Science* 2020; 234: 2279–2293.
49. Free3D, https://free3d.com/3d-model/freerealsichand-85561.html (accessed 7 July 2019).
50. Cosmi F and Tomanik M. Preliminary design of an x-ray imaging system for the bone structure index evaluation. *Mater Today: Proc* 2016; 3: 947–952.
51. Tonti E. A direct discrete formulation of field laws: the cell method. *Comput Model Eng Sci* 2001; 1: 11–26.
52. Cosmi F, Dreossi D and Vittur F. Bone mechanical properties estimation with the cell method. In: *Proceedings of 18th DAS on experimental methods in solid mechanics*, Steyr, Austria, 2001.
53. JCGM, International vocabulary of metrology - Basic and general concepts and associated terms (VIM), 2012.
54. Sezer A, Altan L and Özdemir Ö. Multiple comparison of age groups in bone mineral density under heteroscedasticity. *BioMed Res Int* 2015; 2015: 1–7.
55. Kim H and Yang S. Quality control of DXA system and precision test of radio-technologists. *J Bone Metab* 2014; 21: 2–7.
56. Macdonald HM, McGuigan FE, Stewart A, et al. Large-scale population-based study shows no evidence of association between common polymorphism of the VDR gene and BMD in British women. *J Bone Miner Res* 2006; 21: 151–162.
57. Binkley N, Kiebzak GM, Lewiecki M, Krueger D, et al. Recalculation of the NHANES database SD improves T-score agreement and reduces osteoporosis prevalence. *J Bone Miner Res* 2004; 20: 195–201.
58. Osteoporosis and Bone Physiology: T and Z scores. 27 July. https://courses.washington.edu/bonephys/opbmdtz.html (2011, accessed 14 November 2019).